

MoRe-3DGS: Motion-resolved reconstruction framework for free-breathing pulmonary MRI based on 3D Gaussian representation

Tengya Peng¹, Ruyi Zha², Qing Zou^{3,4,5}

¹Department of Biomedical Engineering, University of Texas Southwestern Medical Center, Dallas, TX, USA

²Australian National University, Canberra, Australia

³Department of Pediatrics, University of Texas Southwestern Medical Center, Dallas, TX, USA

⁴Department of Radiology, University of Texas Southwestern Medical Center, Dallas, TX, USA

⁵Advanced Imaging Research Center, University of Texas Southwestern Medical Center, Dallas, TX, USA

E-mail: Qing.Zou@UTSouthwestern.edu

Abstract. *Objective:* This study presents an unsupervised, motion-resolved reconstruction framework for high-resolution, free-breathing pulmonary magnetic resonance imaging (MRI), utilizing a three-dimensional Gaussian representation (3DGS).

Approach: The proposed method leverages 3DGS to address the challenges of motion-resolved 3D isotropic pulmonary MRI reconstruction by enabling data smoothing between voxels for continuous spatial representation. Pulmonary MRI data acquisition is performed using a golden-angle radial sampling trajectory, with respiratory motion signals extracted from the center of k-space in each radial spoke. Based on the estimated motion signal, the k-space data is sorted into multiple respiratory phases. A 3DGS framework is then applied to reconstruct a reference image volume from the first motion state. Subsequently, a patient-specific convolutional neural network is trained to estimate the deformation vector fields (DVF), which are used to generate the remaining motion states through spatial transformation of the reference volume. The proposed reconstruction pipeline is evaluated on six datasets from six subjects and bench-marked against three state-of-the-art reconstruction methods.

Main results: The experimental findings demonstrate that the proposed reconstruction framework effectively reconstructs high-resolution, motion-resolved pulmonary MR images. Compared with existing approaches, it achieves superior image quality, reflected by higher signal-to-noise ratio and contrast-to-noise ratio.

Conclusion: The proposed unsupervised 3DGS-based reconstruction method enables accurate motion-resolved pulmonary MRI with isotropic spatial resolution. Its superior performance in image quality metrics over state-of-the-art methods highlights its potential as a robust solution for clinical pulmonary MR imaging.

Keywords: Pulmonary MRI, Motion-resolved, 3D Gaussian representation, Ultra-short echo time sequence, Non-Cartesian MRI

1. Introduction

Magnetic resonance imaging (MRI) holds significant promise for the evaluation of pulmonary diseases, owing to its superior soft tissue contrast and ability to delineate structural details of the lungs [1, 2, 3]. However, pulmonary MRI is technically challenging due to the inherently short T_2^* relaxation time of lung tissue and the presence of respiratory motion artifacts. To address the rapid signal decay associated with short T_2^* , specialized pulse sequences such as ultrashort echo time (UTE) [4, 5] and zero echo time (ZTE) [6, 7] have been developed. These sequences utilize optimized excitation schemes and fast readout trajectories to achieve sub-millisecond echo times (TE), thereby enhancing signal-to-noise ratio (SNR) in lung imaging.

Most UTE and ZTE implementations adopt non-Cartesian k-space trajectories, such as three-dimensional (3D) radial sampling, to maximize sampling efficiency and improve robustness to motion [8, 9, 10]. In particular, center-out 3D radial acquisitions with golden-angle rotation have become increasingly popular due to their ability to facilitate rapid data acquisition and enable high-quality image reconstruction [11, 12]. Moreover, the retrospective sorting capability of 3D radial sampling provides additional flexibility to implement motion compensation reconstruction algorithms [13, 14]. Despite these advances, high-resolution 3D UTE/ZTE acquisitions typically require several minutes of scan time, during which respiratory motion can degrade image quality through motion-induced artifacts, even when non-Cartesian sampling is used. To mitigate motion artifacts, respiratory signals can be acquired using external devices such as respiratory belts, which monitor abdominal expansion during respiration. But such signal from external devices can be unreliable in some cases [15]. Alternatively, self-navigation methods exploit the repeatedly sampled center of k-space, also known as the direct current (DC) signal, to estimate respiratory motion directly from the MRI data. This approach is particularly compatible with center-out UTE sequences and enables motion tracking without the need for external hardware.

Respiratory motion signals extracted from self-navigation techniques enable retrospective sorting of k-space data into discrete respiratory phases, thereby facilitating motion-resolved image reconstruction. Traditional reconstruction strategies primarily rely on compressed sensing (CS) methodologies [16], wherein initial reconstructions – typically obtained via inverse Fourier transforms – are iteratively refined through low-rank or sparsity-based regularization. These methods aim to suppress noise and artifacts while preserving critical anatomical structures. One notable example is XD-GRASP (eXtra-Dimensional Golden-angle RAdial Sparse Parallel imaging) [17], which integrates compressed sensing with parallel imaging using multi-dimensional encoding and temporal gradient sparsity to accelerate reconstruction and reduce sampling requirements. More recently, ExtremeMRI [18] proposed a multiscale low-rank (MSLR)

factorization model, representing the spatiotemporal data matrix as a summation of block-wise low-rank matrices across multiple scales, and optimized the model using stochastic gradient methods. With the emergence of deep learning, newer approaches have unrolled the iterative optimization steps of CS into trainable neural network frameworks [19, 20], while such methods usually requires extensive training data for network training, which is usually not feasible in the setting of 3D non-Cartesian MRI. An alternative paradigm, which is usually done in an unsupervised fashion, involves directly treating the MR volume representation as a learnable parameter. In this formulation, model parameters are optimized by backpropagating through the Fourier transform to minimize the discrepancy between predicted and acquired k-space data. For instance, the work of MoCo-SToRM [21] introduced a method in which a learnable tensor encodes the dynamic MR volume, and a neural decoder is used to predict deformation vector fields (DVF) [22], enabling the transformation of a reference image into various motion states.

Three-dimensional Gaussian representation (3DGS) has recently emerged as a powerful technique for scene representation and novel view synthesis [23], owing to its ability to model complex 3D structures with high fidelity through the smooth and continuous nature of Gaussian distribution functions [24]. In this framework, these distribution functions –hereafter referred to as Gaussian points – serve as spatially localized primitives that encode both geometric and radiometric properties. Each Gaussian point is characterized by attributes such as position, anisotropic scale, and orientation, which collectively influence its contribution to the overall rendered scene. By capturing spatial correlations within a probabilistic representation, 3DGS facilitates efficient and accurate modeling of three-dimensional environments. The strengths of 3DGS have recently been extended to medical imaging applications. Zha et al.[25] successfully employed 3D Gaussian splatting for cone-beam computed tomography (CBCT) reconstruction. In this work, we further adapt and extend the voxelizer to accommodate the complex-valued nature of MRI data, as opposed to the real-valued setting typical of X-ray and CBCT modalities.

The primary aim of this study is to integrate respiratory motion information into the 3DGS framework for motion-resolved reconstruction of pulmonary MRI. To achieve this, respiratory motion signals were first estimated from the center of k-space data, enabling retrospective binning of the k-space into a fixed number of discrete motion states. The first motion state, designated as the reference state, was reconstructed using 3DGS. To enhance the convergence and stability of the reconstruction process, a novel multi-resolution scaled initialization strategy was introduced. Simultaneously, a convolutional decoder network was trained to estimate deformation vector fields (DVF), which were subsequently applied to the reference state to generate the remaining motion states via spatial transformation. For each motion state, a non-uniform fast Fourier transform (NUFFT) was performed to simulate corresponding k-space data, which was then compared against the actual binned k-space data for that respiratory phase to enforce data consistency during training.

2. Methods

2.1. 4D MRI reconstruction from radial sampling

The 4D MRI reconstruction (a.k.a motion-resolved reconstruction) of free-breathing, ungated 3D pulmonary MRI acquired using center-out radial sampling begins with the estimation of respiratory motion from the central k-space data, commonly referred to as the DC signal. In this study, respiratory motion estimation was performed following the methodology outlined in [26]. Specifically, the multi-coil k-space data were first combined using the adaptive navigator strategy [27]. The resulting DC signals were subsequently processed using a low-pass filter with a cutoff frequency between 0.5 and 1 Hz to attenuate high-frequency noise components.

Following motion signal estimation, the k-space data were retrospectively sorted into N respiratory motion states, ranging from end-expiration to end-inspiration. The proposed motion-resolved reconstruction framework is formulated as a learning task that jointly estimates an image representation \mathbf{X} corresponding to the reference motion state (defined as the first respiratory phase in this work), and a motion decoder D_θ which outputs deformation vector fields $v_t = D_\theta(t)$ for each respiratory phase index $t = 1, \dots, N$. The reference image representation \mathbf{X} can then be optimized by solving a data fidelity-driven minimization problem that enforces consistency with the acquired motion-binned k-space measurements:

$$\arg \min_{\mathbf{X}, \theta} \sum_t \|F \cdot C \cdot \text{warp}(\mathbf{X}, D_\theta(t)) - m_t\| + \lambda_{tv} \cdot TV(\mathbf{X}). \quad (1)$$

Here, the warp function is implemented using a spatial transformer [28]. F is the NUFFT operator and C is the coil sensitivity maps. $m_t = [m_1, \dots, m_N]^T$ represents the sorted k-space data for the N motion states. θ denotes the decoder network parameters. TV represents the total variation regularization term [29] to further regularize the reconstructed images and λ_{tv} is the balancing parameter to balance the data consistency term and the regularization term.

2.2. 3D Gaussian representation for 3D MRI

In this work, we represent the reference image representation $\mathbf{X} = [\mathbf{x}_j]$ with $\mathbf{x}_j \in \mathbb{C}$ in equation (1) using 3DGS. Specifically, we represent each \mathbf{x}_j as a linear combination of a set of Gaussian points. Mathematically speaking,

$$\mathbf{x}_j = \sum_{i=1}^M G_i^3(\mathbf{j} | \rho_i, \mathbf{p}_i, \Sigma_i), \quad (2)$$

where M is the number of Gaussian points to represent each voxel and

$$G_i^3(\mathbf{j} | \rho_i, \mathbf{p}_i, \Sigma_i) = \rho_i \cdot \exp\left(-\frac{1}{2}(\mathbf{j} - \mathbf{p}_i)^T \Sigma_i^{-1} (\mathbf{j} - \mathbf{p}_i)\right). \quad (3)$$

Here, $\mathbf{j} = (x_j, y_j, z_j)$ is the spatial location for each voxel in the image volume and \mathbf{p}_i is the center location of the each Gaussian point. ρ_i is a complex number to represent the central density value of the Gaussian point. Σ_i defines the shape size and orientation of the Gaussian point, and can be represented as

$$\Sigma_i = \mathbf{R}_i \mathbf{S}_i \mathbf{S}_i^T \mathbf{R}_i^T, \quad (4)$$

where R_i and S_i represents the rotation and scaling matrix respectively. The rotation matrix is represented by pairs of iso-rotations characterized by quaternions. The scaling matrix quantifies the size of Gaussian points in three directions.

In (2), each Gaussian point is characterized by a set of learnable parameters, including its spatial scale, anisotropic orientation, and central density value. Each Gaussian point exerts influence over a localized region within the volume, specifically within a radius of 3σ , where σ denotes the length of the principal axis of the corresponding Gaussian ellipsoid. This localized influence allows the 3DGS to compactly model complex 3D structures while maintaining accurate spatial continuity and smoothness. Furthermore, Equation (2) defines the voxelization process, which maps the continuous 3D Gaussian point cloud into a discretized voxel grid, thereby enabling integration with conventional volumetric processing pipelines.

Adaptive control [30] serves as a key component in the original 3DGS framework, facilitating the dynamic densification of Gaussian points. This process enhances the representational capacity and structural fidelity of the reconstruction by incrementally introducing additional Gaussian points. However, in this work, an ablation study demonstrated that initializing the reconstruction with the maximum number of Gaussian points, while omitting the adaptive densification process, resulted in improved training efficiency without compromising reconstruction quality. Consequently, adaptive control was omitted in this work.

2.3. Multi-resolution Initialization Strategy

Accurate initialization plays a critical role in ensuring effective performance in 3D Gaussian-based reconstruction frameworks [31], which involves generating the initial 3D Gaussian points based on the inverse NUFFT of the motion-sorted radial k-space data corresponding to the first respiratory state. Random initialization remains a commonly adopted approach in existing literature [23, 25], where the spatial positions of the Gaussian points are randomly sampled within the volume. Their initial scales are computed as the average distance to their three nearest neighboring Gaussian points. As a result, the initialized Gaussian points exhibit variability in both spatial location and scale.

It has been demonstrated in previous research [32] that equal-space initialization yields superior performance in the context of reconstruction from undersampled data, primarily due to the enhanced capability of uniformly distributed, small-scale Gaussian points to capture high-frequency image components. In this initialization strategy,

Gaussian points are initialized with approximately equal inter-point spacing and consistent scale parameters. This uniform configuration facilitates faster convergence towards accurate representation.

In this study, a multi-resolution initialization strategy is proposed to enhance the representation capability of 3DGS for motion-resolved MRI reconstruction, due to the nature of radial k-space sampling and the amount of k-space in each motion states. In contrast to the existing coarse-to-fine training paradigm that trains Gaussian points with densification progressively from low resolution to high resolution, the proposed multi-resolution initialization strategy initializes Gaussian points based on the frequency domain information, progressing from coarse-to-fine, and then the initialized Gaussian points with different sizes are trained simultaneously. Specifically, inverse NUFFT operations are applied to frequency-filtered k-space data across multiple resolution levels, forming a resolution pyramid. At each level, Gaussian points are initialized using an equal-space initialization. Larger Gaussian points are allocated to low-frequency components to capture coarse anatomical structures, while smaller Gaussian points are assigned to high-frequency components to preserve fine-grained details. This initialization method is depicted in Figure 1. By enabling simultaneous training of Gaussian points across multiple resolution levels during training, this approach eliminates the need for a separate coarse-to-fine training phase with adaptive densification.

2.4. Motion correction

In motion-resolved reconstruction, k-space data are retrospectively sorted into N uniformly sorted respiratory phases based on the estimated motion signal, covering the full respiratory cycle from end-inspiration to end-expiration. In the proposed framework, motion correction is achieved through a convolutional decoder network D_θ that estimates deformation vector fields (DVF) wrapping the first motion state, which is the reference motion states, to the rest of the motion states. The detailed structure of D_θ is shown in Table 1. The layer sizes gradually increase until they reach the specified image dimensions. To enhance the network’s representation capacity, more features are utilized in the initial layers, while the number of features is reduced in the final layers to maintain a low memory footprint for the generator. The decoder receives motion indices $t = 1, \dots, N$ as input and outputs the corresponding DVFs for the motion states. Architecturally, the decoder is composed of convolutional layers with Leaky ReLU activation functions. The learned DVFs are optimized to deform the reference motion state in such a way that the resulting transformed volumes accurately reconstruct the remaining motion states.

2.5. MoRe-3DGSMR

Integrating the aforementioned components yields the proposed motion-resolved reconstruction framework for isotropic-resolution 3D pulmonary MRI, referred to as

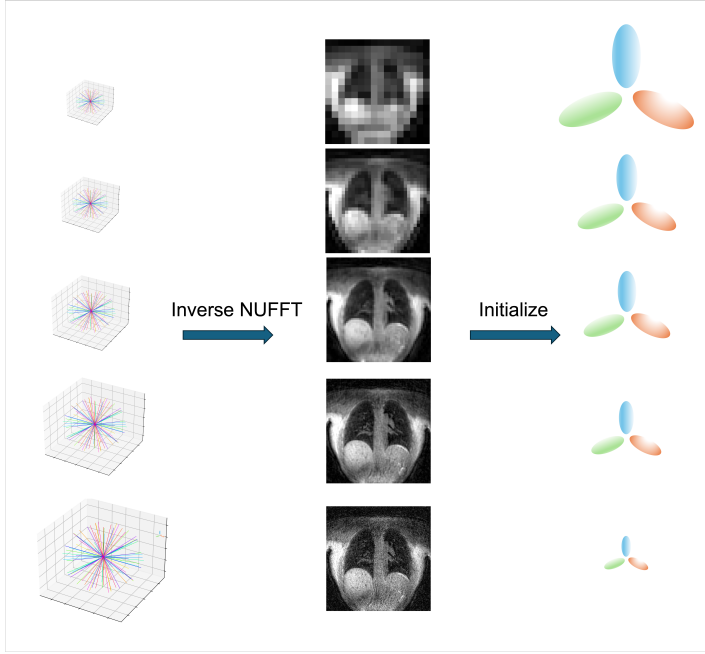


Figure 1. Illustration of the multi-resolution initialization strategy. Gaussian points are initialized at multiple spatial scales using outputs from inverse Fourier transforms computed at progressively increasing levels of k-space coverage, forming a hierarchical (pyramidal) architecture. Each resolution level corresponds to a subset of the k-space data, with higher levels incorporating a greater number of samples per radial spoke to progressively recover higher-frequency information. The Gaussian points initialized at each level are summed, and then simultaneously refined during the training process.

MoRe-3DGSMR. The overall reconstruction pipeline is depicted in Figure 2. In this framework, the proposed 3DGS framework described above is employed to reconstruct the reference motion state (i.e., the first respiratory phase). The subsequent motion states are generated by warping the reference motion state using the DVFs predicted by the convolutional decoder. For each motion state, the corresponding k-space data are computed using the NUFFT operator. Model optimization is done by minimizing the discrepancy between the computed k-space and the motion-sorted k-space measurements. This is achieved by back-propagating the loss through the entire pipeline, thereby updating the parameters of the Gaussian points and the decoder network. The overall loss function used for motion-resolved reconstruction is then defined as follows:

$$\mathcal{L}(\rho_i, \mathbf{p}_i, \Sigma_i, \theta) = \sum_t \left\| F \cdot C \cdot \text{warp} \left(\sum_{i=1}^M G_i^3(\mathbf{j}|\rho_i, \mathbf{p}_i, \Sigma_i), D_\theta(t) \right) - m_t \right\| + \lambda_{tv} \cdot TV \left(\sum_{i=1}^M G_i^3(\mathbf{j}|\rho_i, \mathbf{p}_i, \Sigma_i) \right).$$

The Gaussian points and the decoder network are optimized simultaneously by minimizing the loss function.

Table 1. Structure of the Decoder D_θ to Predict DVFs

Layer	Filter size	Kernel size	Stride	Padding
Conv3d + Tanh	30	1	1	0
Conv3d + LeakyReLU	400	3	1	1
Upsample (factor=2)	—	—	—	—
Conv3d + LeakyReLU	200	3	1	1
Upsample (factor=2)	—	—	—	—
Conv3d + LeakyReLU	200	3	1	1
Upsample (factor=2)	—	—	—	—
Conv3d + LeakyReLU	100	3	1	1
Upsample (factor=2)	—	—	—	—
Conv3d + LeakyReLU	50	3	1	1
Upsample (factor=2)	—	—	—	—
Conv3d + LeakyReLU	50	3	1	1
Upsample (factor=2)	—	—	—	—
Conv3d + LeakyReLU	50	3	1	1
Upsample (factor=2)	—	—	—	—
Conv3d + LeakyReLU	50	3	1	1
Upsample (factor=2)	—	—	—	—
Conv3d + LeakyReLU	3	3	1	1
Upsample (factor=2)	—	—	—	—

Once the Gaussian points and the convolutional decoder are sufficiently trained, the 3DGS is voxelized to obtain the volume representation for the first motion states. The subsequent motion states are obtained by applying the DVFs predicted by the decoder to the first motion state.

2.6. Dataset

Six healthy volunteers were enrolled in this study. The data acquisition protocol was approved by the local Institutional Review Board, and written informed consent was obtained from all participants prior to imaging. All datasets were acquired using a 3D center-out radial UTE sequence on a 3T GE MRI scanner equipped with AIR coils. The imaging protocol employed 86,000 uniformly distributed golden-angle radial spokes, with a repetition time (TR) of 3.7 ms and 149 samples per readout, resulting in a total acquisition time of approximately 5.5 minutes. To reduce data dimensionality while preserving signal quality, a PCA-based coil compression method [33] was applied, retaining eight virtual coils for subsequent reconstruction. The prescribed field of view = $32 \times 32 \times 32 \text{ cm}^3$ and the reconstruction matrix size = $256 \times 256 \times 256$.

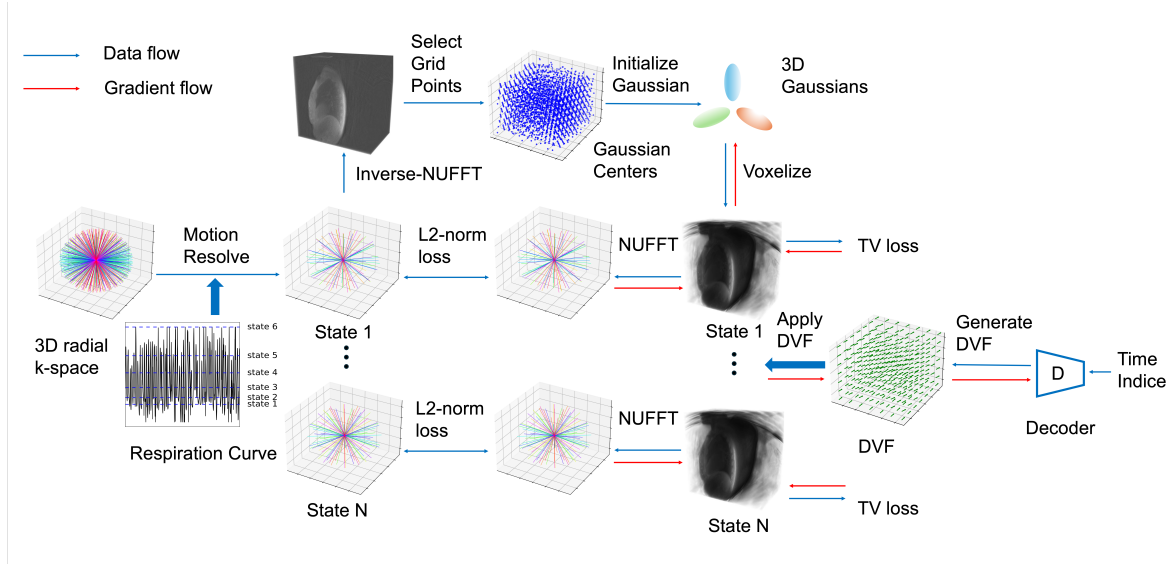


Figure 2. Overall pipeline for MoRe-3DGSMD. The framework comprises the following key components: k-space binning, multi-resolution Gaussian points initialization, voxelization, DVFs prediction, motion warping, and NUFFT operations. The estimated respiratory signal is used to retrospectively sort radial k-space spokes into discrete motion states corresponding to different respiratory phases. The k-space data from the first motion state are utilized for initializing the Gaussian points. During training, these Gaussian points are iteratively optimized and subsequently voxelized into volumetric representations.

2.7. Implementation details

The proposed MoRe-3DGSMD framework was implemented using the PyTorch library, with the SigPy library employed for the NUFFT operation. All experiments were conducted on a single NVIDIA A6000 GPU, which provides 48 GB of memory. Although increasing the number of Gaussian points improves the model’s capacity, it also leads to increased computational demands and longer training durations. Consequently, the maximum number of Gaussian points utilized in this study was constrained by the available GPU memory. The hyper-parameters in the framework are determined by the ablation studies which are described in the following section.

3. Experiments and Results

3.1. Motion fields prediction using convolutional decoder

The proposed framework incorporates a convolutional decoder to directly estimate the DVFs between respiratory motion states. The decoder is composed of convolutional layers designed to capture spatial correlations and predict smooth, anatomically consistent motion fields. Figure 3 presents representative DVFs in the sagittal and coronal planes for a single slice, demonstrating the effectiveness of the convolutional decoder. As expected, the predicted motion fields exhibit coherent motion in the lungs

and diaphragm regions, while the spinal column remains largely static, consistent with physiological behavior. These results confirm that a convolutional-layer-based decoder is sufficient for accurately modeling respiratory motion in the context of motion-resolved MRI reconstruction.

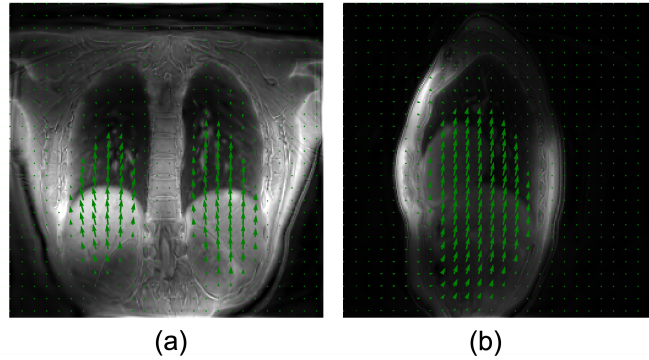


Figure 3. Examples of predicted DVFs. (a) Coronal view. (b) Sagittal view.

3.2. Ablation study

This section presents ablation studies conducted to identify the optimal hyperparameters for the MoRe-3DGSMR framework. The parameters evaluated include the number of initialized Gaussian points, the TV regularization weight λ_{tv} , and the number of motion states used for k-space binning. In addition, we compared the proposed multi-resolution initialization strategy with the existing commonly used baseline methods: random initialization and equal-space initialization. The MoRe-3DGSMR model was trained in a self-supervised manner, without the use of ground truth. To quantitatively evaluate the impact of different hyperparameter settings and initialization strategies, several image quality metrics were computed across the reconstructed image volumes.

To assess image sharpness and detect blurriness in anatomical regions such as the liver, spine, lung, and heart, we introduce the Sobel and Laplacian indices as quantitative evaluation metrics. The Sobel index measures image sharpness by applying the Sobel operator [34], which computes the intensity gradient at each pixel, highlighting spatial variations along the horizontal and vertical directions. These directional gradients are obtained by convolving the image with predefined horizontal and vertical kernels, as defined below:

$$\begin{aligned}
 G_x &= \sum_{k=-1}^1 \sum_{l=-1}^1 I(i, j) * \begin{pmatrix} -1 & 0 & 1 \\ -2 & 0 & 2 \\ -1 & 0 & 1 \end{pmatrix} (k, l) \\
 G_y &= \sum_{k=-1}^1 \sum_{l=-1}^1 I(i, j) * \begin{pmatrix} -1 & -2 & -1 \\ 0 & 0 & 0 \\ 1 & 2 & 1 \end{pmatrix} (k, l)
 \end{aligned} \tag{5}$$

The Sobel index can then be computed by:

$$G = \sqrt{G_x^2 + G_y^2}. \quad (6)$$

A higher Sobel index indicates more pronounced details, while lower values indicate a smoother or more blurred image.

Laplacian index is another image sharpness measurement based on the Laplacian operator [35] that detects regions of rapid intensity change by computing the second derivative of the pixel intensity values. The images are first convolved with the Laplacian kernel, which is defined as follows:

$$L(i, j) = \sum_{k=-1}^1 \sum_{l=-1}^1 I(i, j) * \begin{pmatrix} 0 & 1 & 0 \\ 1 & -4 & 1 \\ 0 & 1 & 0 \end{pmatrix} (k, l). \quad (7)$$

The Laplacian index is then defined as the standard deviation of the convolved outputs:

$$\sigma = \sqrt{\frac{1}{N} \sum_{i=1}^N (L(i, j) - \mu)^2}. \quad (8)$$

A higher Laplacian index indicates more rapid intensity changes, which indicates more detail richness, while lower values indicate potential blurriness.

Signal-to-noise ratio (SNR) and contrast-to-noise ratio (CNR) are also measured to analyze the image quality of the reconstructed images. SNR is calculated as follows:

$$SNR = 20 \log \left(\frac{\mu_{ROI}}{\sigma_{noise}} \right), \quad (9)$$

where \log is the logarithm of base 10, μ_{ROI} is the mean intensity value within the region of interest (ROI), and σ_{noise} is the standard deviation of intensity values of the noise region that is chosen from the background of the images. Similarly, CNR assesses the contrast quality by comparing the difference in intensity values between the ROI and the selected noise regions through

$$CNR = 20 \log \left(\frac{|\mu_{ROI} - \mu_{noise}|}{\sigma_{noise}} \right), \quad (10)$$

where μ_{ROI} and μ_{noise} represent the mean intensity value of ROI and the noise regions while σ_{noise} represents the standard deviation of the intensity values in the noise regions. Different from Sobel and Laplacian indices, SNR and CNR measure the difference between the selected ROI and the noise in the backgrounds.

3.2.1. Number of initialized Gaussian points and number of iterations An ablation study was first performed to investigate the effect of the number of initialized Gaussian points M and the number of training epochs (500, 1000, 1500, and 2000)

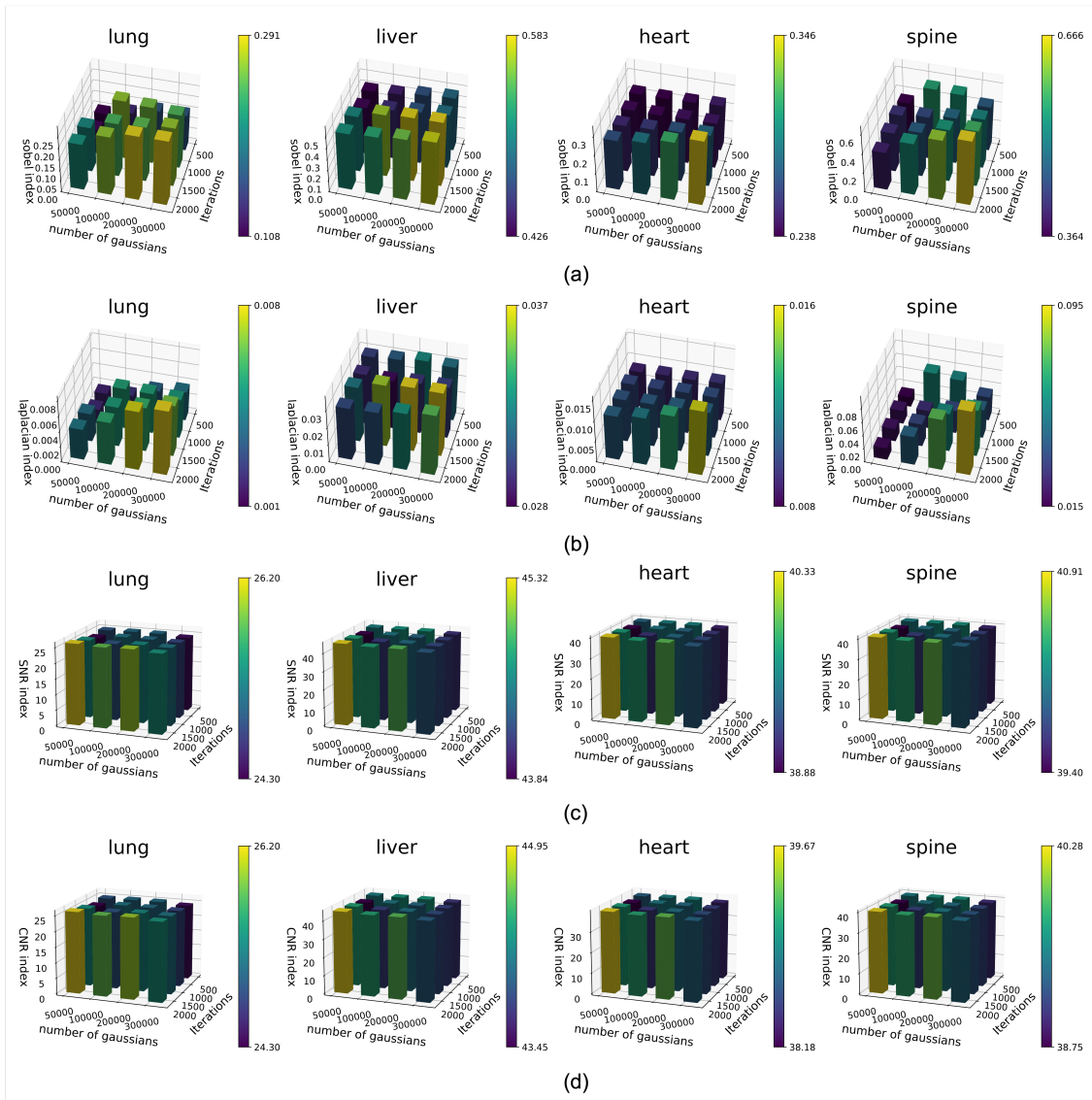


Figure 4. Results of the ablation study investigating the impact of the number of initialized Gaussian points and the number of training iterations are presented. Reconstruction performance was quantitatively evaluated using four metrics – Sobel index, Laplacian index, SNR, and CNR – across four anatomical regions: lung, liver, heart, and spine.

on reconstruction performance, using a fixed number of motion states ($N = 6$) for a representative subject. The maximum number of Gaussian points was constrained to 300,000 due to GPU memory limitations. When initialized with 300,000 Gaussian points, no additional densification was performed during training. To quantitatively assess image quality under different settings, we computed the Sobel index, Laplacian index, SNR, and CNR. The results are presented as bar graphs in Figure 4. The experimental results in Figure 4 indicate that, in most cases, initializing with $M = 300,000$ Gaussian points and training for 2000 iterations yields better image quality, as evidenced by higher Sobel and Laplacian indices as well as improved SNR and

CNR. However, a trade-off was observed: increasing M and the number of training iterations generally enhanced detail-related metrics (Sobel and Laplacian indices) but did not always correspond to proportional improvements in SNR and CNR. Considering this trade-off and based on a comprehensive evaluation of image quality across key anatomical regions including the lungs, liver, heart, and spine, we selected $M = 300,000$ and 2000 training iterations as the optimal configuration for the proposed framework.

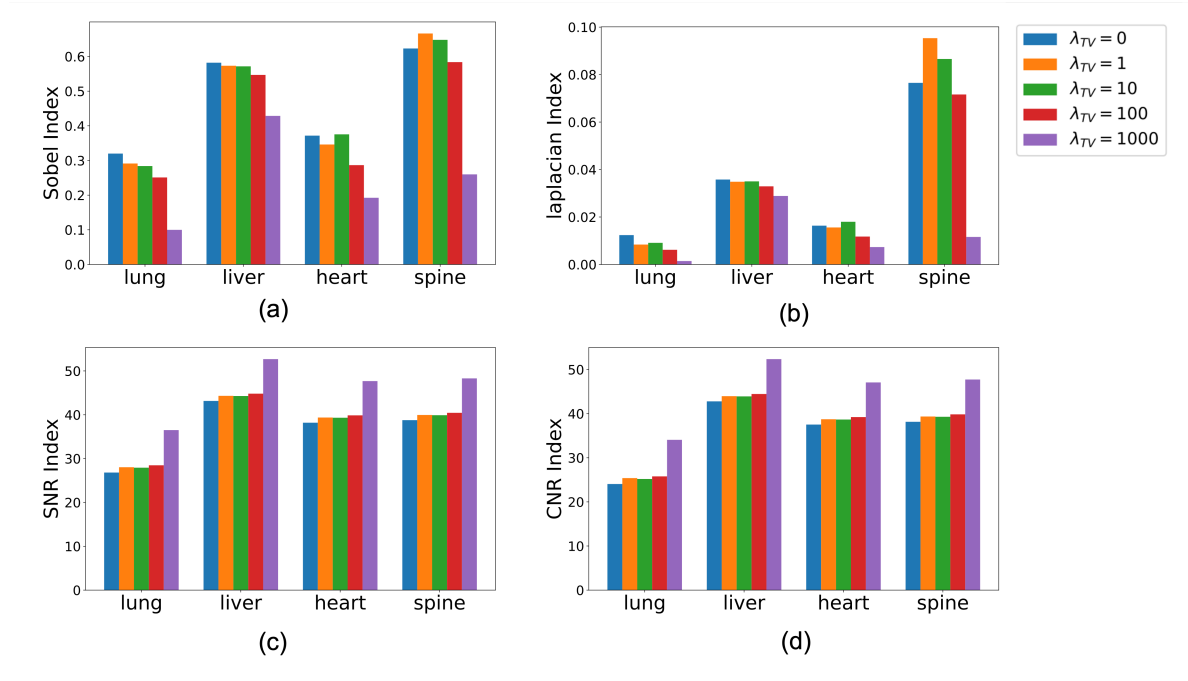


Figure 5. Results of the ablation study evaluating the effect of the hyperparameter λ_{tv} are presented. Quantitative assessments were performed using four evaluation metrics (a) Sobel index, (b) Laplacian index, (c) SNR, and (d) CNR – across four anatomical regions: lung, liver, heart, and spine.

3.2.2. Balancing parameter λ_{tv} for TV regularization An ablation study was conducted to investigate the impact of the TV regularization balancing parameter λ_{tv} on image quality. For this analysis, the number of initialized Gaussian points was fixed at $M = 300,000$, and the number of training iterations was set to 2000. The results are presented in Figure 5. As shown, increasing λ_{tv} leads to an improvement in noise-related metrics, including SNR and CNR, while simultaneously causing a trend of decline in image sharpness, as indicated by the Sobel and Laplacian indices. This behavior aligns with the expected trade-off imposed by TV regularization, which inherently balances noise suppression and edge sharpness. Based on a comprehensive evaluation of reconstructed image quality across anatomical regions, $\lambda_{tv} = 1$ was selected for this study, primarily due to its favorable performance in enhancing structural clarity in the spine region while maintaining acceptable noise levels.

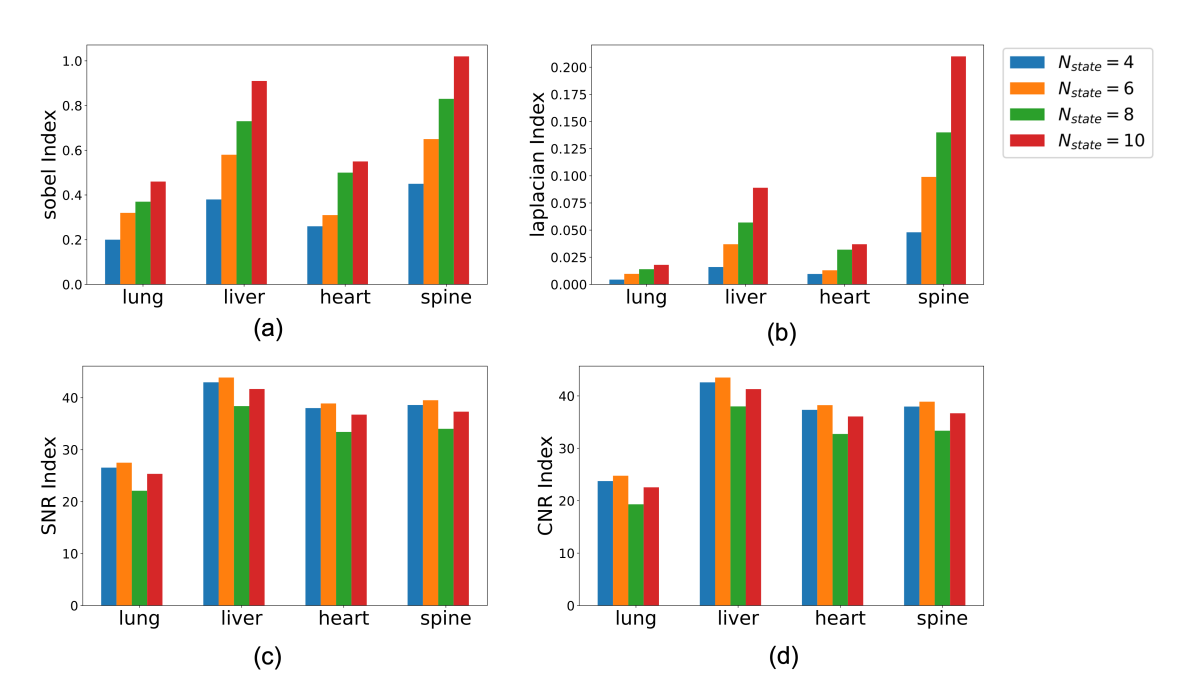


Figure 6. Results of the ablation study evaluating the effect of the number of motion states N_{state} are presented. Quantitative assessments were performed using four evaluation metrics (a) Sobel index, (b) Laplacian index, (c) SNR, and (d) CNR – across four anatomical regions: lung, liver, heart, and spine.

3.2.3. Effects of number of motion states N_{state} In the proposed motion-resolved reconstruction framework, the acquired k-space data are retrospectively and uniformly sorted into N_{state} respiratory motion states based on the estimated motion signal. This section investigates the influence of the number of motion states, N_{state} , on the quality of the reconstructed images. Quantitative results are presented in Figure 6. As shown, the configuration with $N_{state} = 6$ achieves the highest SNR and CNR. Although increasing N_{state} improves motion resolution, evidenced by enhanced Sobel and Laplacian indices. However, increasing N_{state} also reduces the number of k-space samples per motion state, potentially introducing undersampling artifacts and degrading overall image quality. Therefore, $N_{state} = 6$ was selected as the optimal setting, offering a favorable trade-off between motion resolution and noise performance. Additionally, representative images across different motion states for varying N_{state} values are shown in Figure 7 to further illustrate the effect of motion binning granularity. A visual comparison of reconstruction quality for different N_{state} values is provided in Figure 8, focusing on the first motion state and including zoomed-in regions for detailed inspection.

3.2.4. Multi-resolution initialization strategy for MoRe-3DGSMD In this work, a multi-resolution initialization strategy was introduced within the MoRe-3DGSMD framework to enhance reconstruction performance. The effectiveness of this strategy was evaluated through both quantitative metrics (Table 2) and qualitative visual

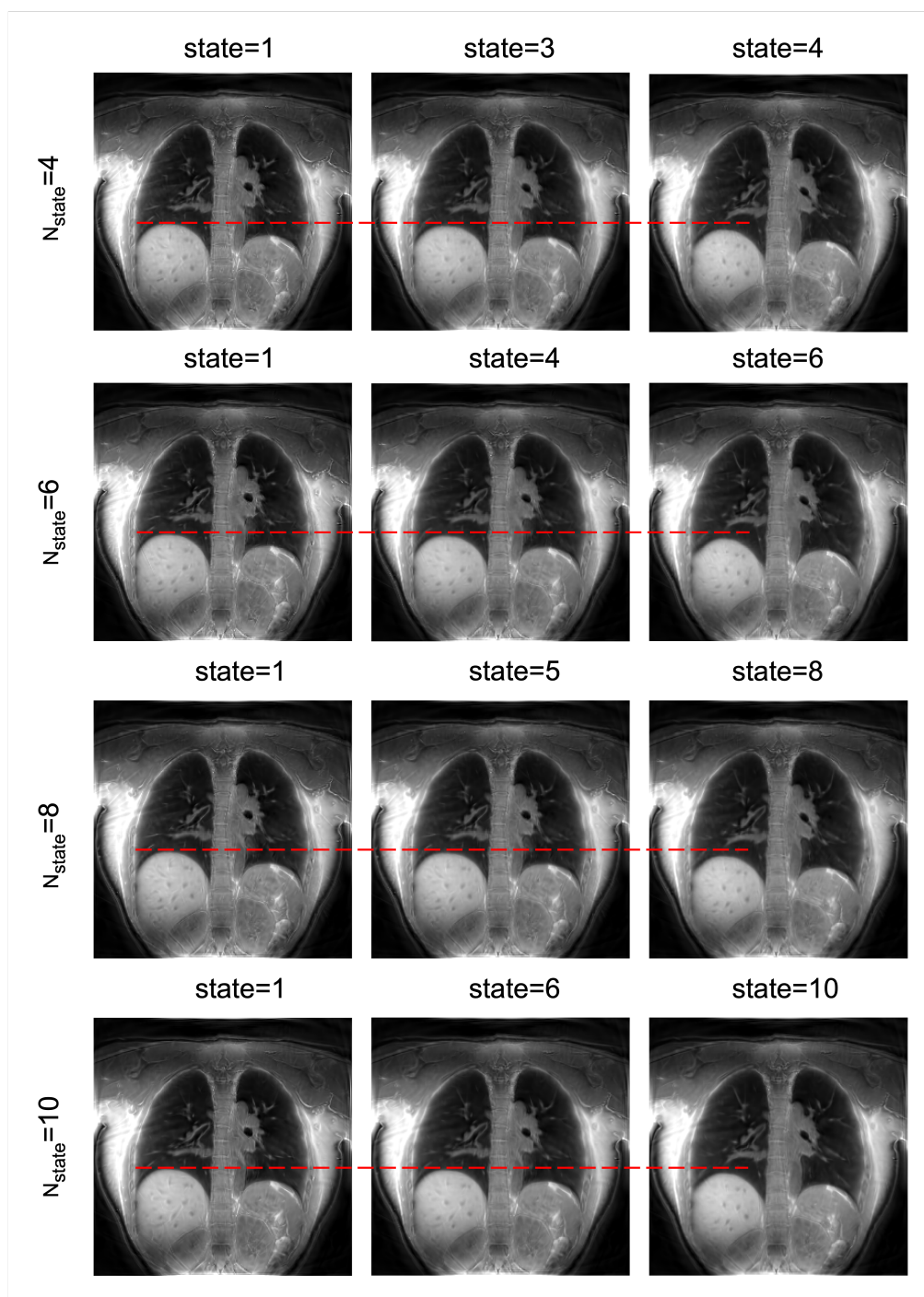


Figure 7. Visual comparisons from the ablation study evaluating the number of motion states (N_{state}) are presented. In each row, three reconstructed motion states corresponding to different phases of the respiratory cycle—end-inspiration, mid-respiration, and end-expiration—are shown to illustrate the temporal consistency and image quality across respiratory phases.

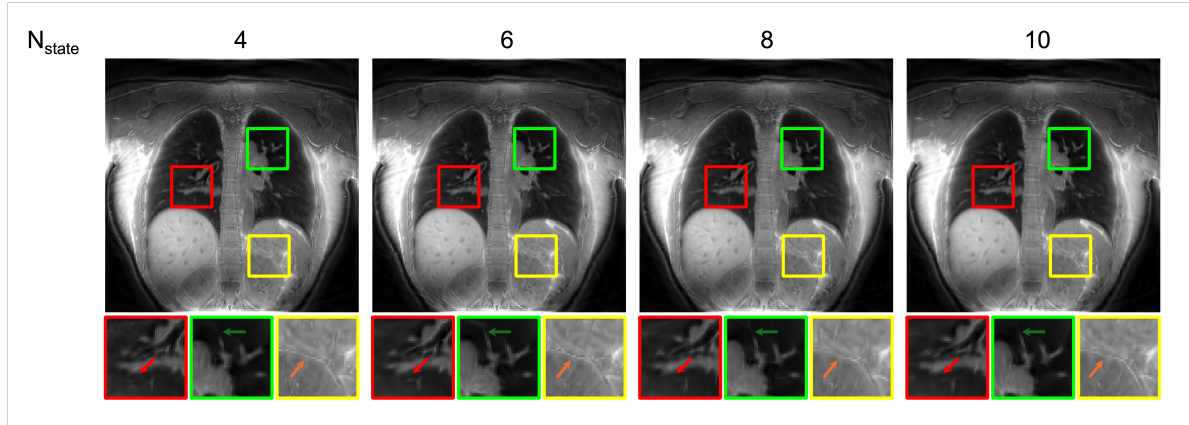


Figure 8. Visual comparison of the ablation study examining the number of motion-resolved phases (N_{state}) is presented. The reconstructed reference phase is included for direct comparison. Selected regions are zoomed in to facilitate detailed evaluation of structural preservation and image quality across different motion state configurations.

organ	Initialization	Sobel	Laplacian	SNR	CNR
lung	Random	0.31	0.0084	26.57	23.90
	Equal-space	0.29	0.0093	26.63	23.88
	Multi-resolution	0.29	0.0099	27.13	24.43
liver	Random	0.57	0.035	42.85	42.49
	Equal-space	0.58	0.035	43.05	42.69
	Multi-resolution	0.59	0.041	43.49	43.13
heart	Random	0.36	0.017	37.90	37.25
	Equal-space	0.37	0.018	38.09	37.43
	Multi-resolution	0.35	0.015	38.45	37.79
spine	Random	0.64	0.084	38.48	37.88
	Equal-space	0.65	0.091	38.66	38.05
	Multi-resolution	0.63	0.086	39.14	38.54

Table 2. Quantitative evaluation of initialization strategies for the MoRe-3DGSMR framework.

comparisons (Figure 9). The results consistently demonstrate the superiority of the proposed initialization approach. Specifically, Table 2 shows that the multi-resolution strategy yields improvements in SNR and CNR, while maintaining comparable Sobel and Laplacian indices relative to other commonly used initialization methods. Furthermore, the visual assessment presented in Figure 9 reveals enhanced preservation of fine anatomical details when using the multi-resolution initialization, further validating its advantage for high-fidelity reconstruction.

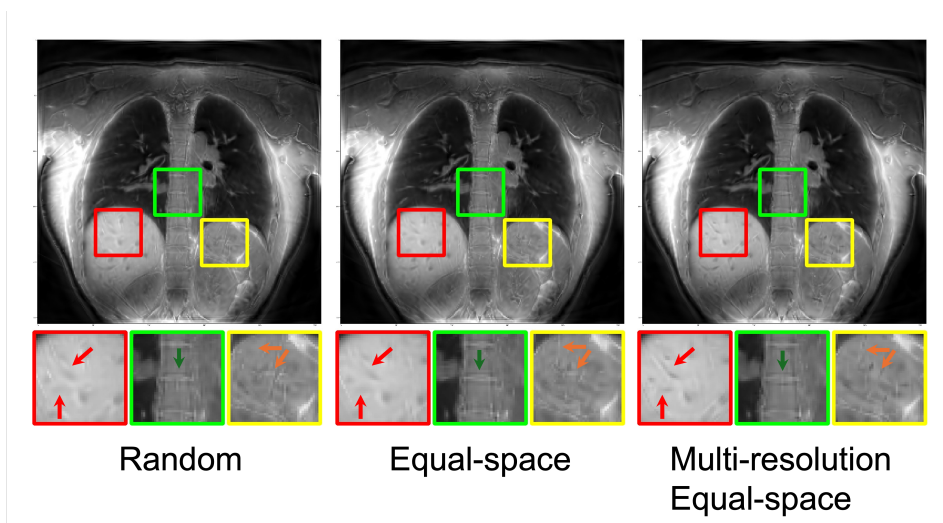


Figure 9. Visual comparisons from the ablation study on initialization strategies are presented. Detailed evaluations are performed on the reconstructed reference phase, with selected regions zoomed in to highlight differences in structural preservation and image quality.

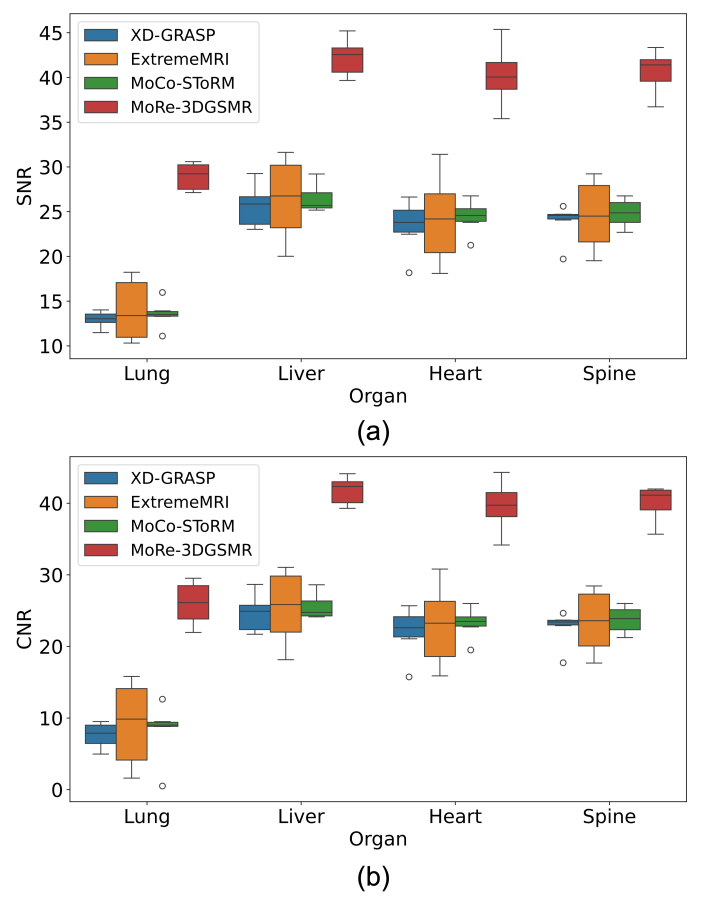


Figure 10. Quantitative comparisons of different reconstruction methods in lungs, livers, hearts, and spines. (a) SNR, (b) CNR.

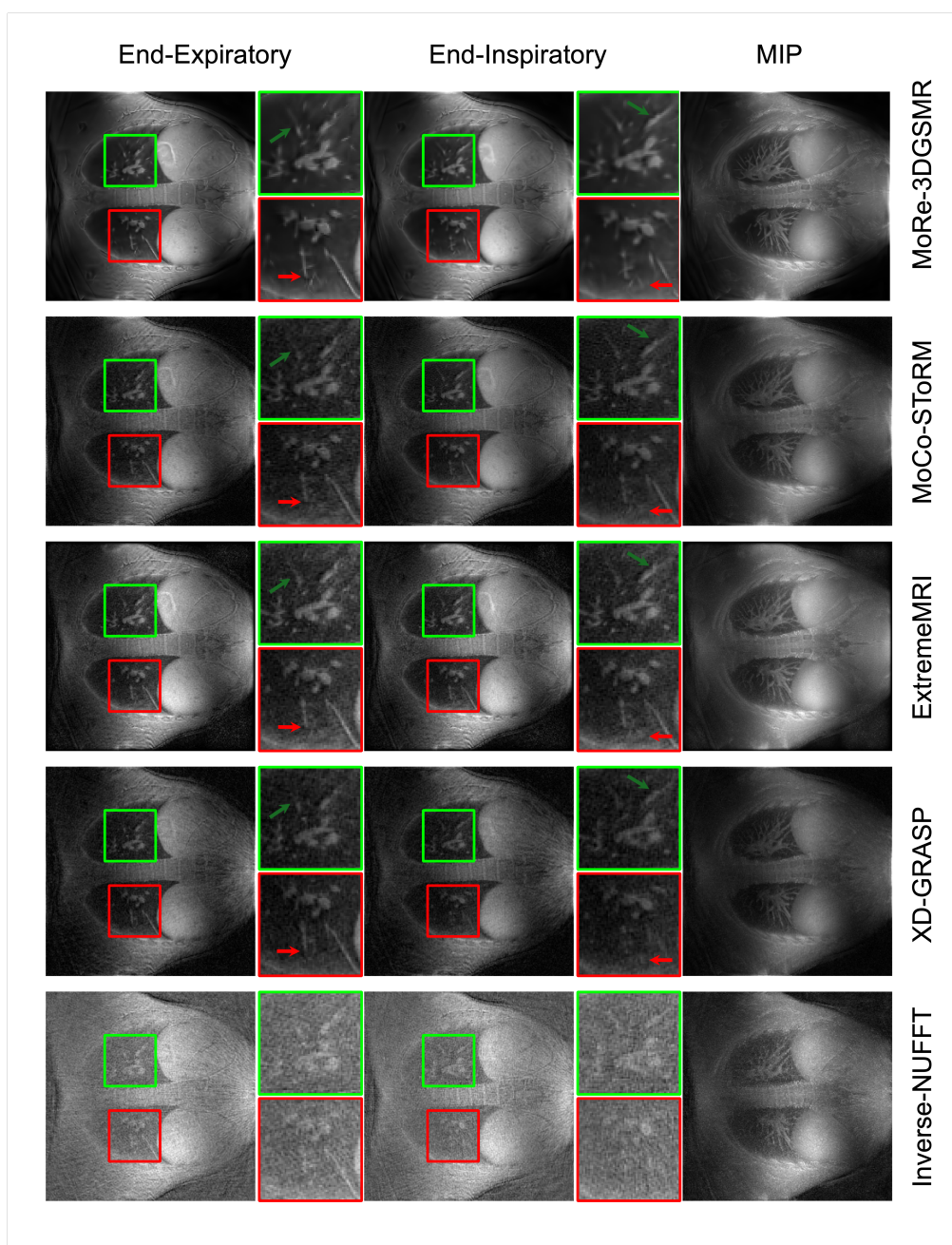


Figure 11. Visual comparisons between the proposed method and competing reconstruction approaches are presented. For each method, coronal slices corresponding to the end-expiratory and end-inspiratory phases are shown. Zoomed-in regions highlight the superior image quality achieved by the proposed method, particularly in preserving fine anatomical details. Additionally, maximum intensity projection (MIP) reconstructions of the central 20 slices are provided for all methods to further illustrate overall structural clarity and contrast.

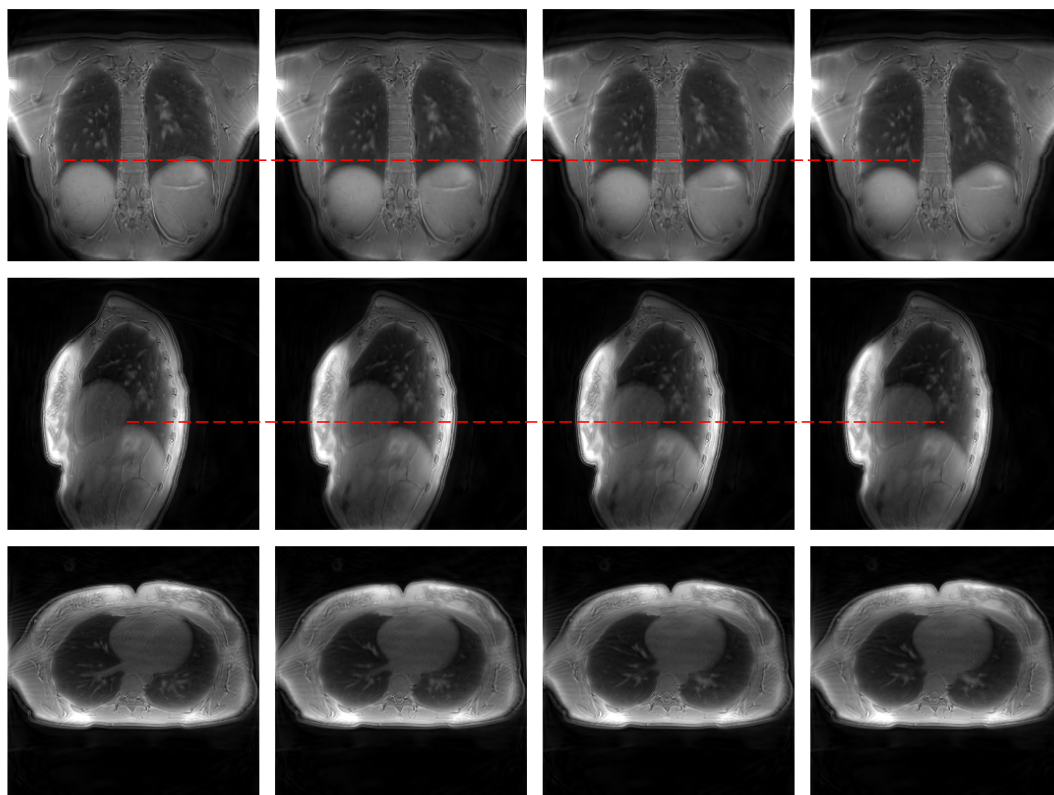


Figure 12. Showcase of reconstruction results on a representative subject in coronal, sagittal, and axial planes.

3.3. Comparison with the state-of-the-art methods

In this section, the proposed MoRe-3DGSMR reconstruction framework is evaluated against three state-of-the-art dynamic MRI reconstruction methods: XD-GRASP, ExtremeMRI, and Moco-SToRM. Quantitative comparisons were conducted using SNR and CNR metrics across four anatomical regions: lung, liver, heart, and spine. The results are summarized in Figure 10, where the boxplots indicate that the proposed method consistently outperforms the baseline methods in terms of both SNR and CNR.

Additionally, a qualitative comparison for a representative subject is presented in Figure 11. The visual results demonstrate that MoRe-3DGSMR produces reconstructions with reduced noise levels and improved depiction of fine structural details. Regions with noticeable enhancements are highlighted using red and green arrows, further underscoring the superior visual fidelity of the proposed framework relative to existing techniques.

3.4. Showcase of MoRe-3DGSMMR

This section presents representative reconstructed images from four respiratory motion states in three anatomical orientations for a single subject, as shown in Figure 12. Respiratory motion is visibly captured through the displacement of the diaphragm across phases. Importantly, the reconstructed image quality remains consistently high across all orientations and motion states. Pulmonary vasculature is clearly delineated with excellent visibility, demonstrating the framework’s ability to preserve fine structural details throughout the respiratory cycle.

4. Discussion

This study proposed an innovative motion-resolved reconstruction framework for the reconstruction of 3D isotropic resolution pulmonary MRI using 3DGS framework, leveraging its effectiveness in adaptive smoothing and interpolation as well as its powerful spatial reconstruction to remove motion and undersampling artifacts. Based on the estimated motion signal from the center k-space, the k-space with radial sampling trajectories is divided into six motion states, each containing an equal number of radial k-space spokes. While such k-space division may introduce few motion artifacts since respiration is not perfectly periodic in reality, the power of 3DGS may help smooth out these motion discrepancies, thereby reducing the resulting artifacts.

Since the Fourier transform of a Gaussian distribution remains a Gaussian distribution, the Fourier transform of MR images voxelized from the combination of 3D Gaussian points should also result in the combination of corresponding 3D Gaussian points in the frequency domain. Therefore, a well-designed undersampling scheme in the frequency domain can still effectively predict these Gaussian points combinations. This is the strength of 3DGS in MRI reconstruction. This study further confirms that this paradigm remains effective in non-Cartesian radial sampling MRI reconstruction, where combinations of Gaussian distributions in the frequency domain can still be predicted to fit the undersampled non-Cartesian radial k-space.

In this study, an innovative multi-resolution initialization framework for 3DGS was proposed. Such initialization strategy initializes the maximum allowed Gaussian points in an equal-space fashion at different levels of resolutions. In this way, coarse-to-fine details are trained meanwhile, accelerating the convergence and improved the reconstruction performance. Pyramid structures are widely adopted in computer vision to account for different resolution levels [36, 37]. Few studies have explored the multi-resolution framework for 3DGS framework [38, 39]. In computer vision, existing research in 3DGS primarily focuses on the densifying strategy within adaptive control. However, few studies in computer vision [31, 40, 41] have proposed the coarse-to-fine training paradigm, which initially trains on low-resolution components and progressively integrates higher-resolution data. These studies typically used down-sampled to fine ground-truth images from sparse views for training, which specifically

applied the multi-resolution framework in the image space. According to medical imaging processing theory, the distinction between downsampled images and their high-resolution counterparts is found in the residual frequency components [42]. This indicates the previous coarse-to-fine training paradigm is equivalent to fitting Gaussian points towards higher resolution components in the frequency space, making the scales of Gaussian distributions smaller. Inspired by this, we initialized several levels of Gaussian points in the initial stage to train them together. Our multi-resolution initialization strategy successfully applies the same concept to 3DGS for the first time in MRI reconstruction.

In this study, it is observed that the TV regularization enhanced the performance in the spine region, where small details are abundant. This suggests that Gaussian points can converge to sizes even smaller than a voxel or two, helping to preserve fine details during reconstruction. While the multi-resolution initialization yielded slightly worse results in the spine region due to the reduced number of smaller Gaussian points in the framework.

5. Conclusion

In this work, a motion-resolved reconstruction framework is proposed by extending the 3DGS framework to 3D non-Cartesian radial pulmonary MRI reconstruction. The results of the study outperform existing baseline reconstruction methods, highlighting the potential of the proposed framework in MRI reconstruction. The proposed reconstruction method is able to reconstruct images with more fine details in different structures and organs, highlighting the clinical potential of the proposed framework in pulmonary MRI.

References

- [1] H. Hatabu, Y. Ohno, W. B. Geftter, G. Parraga, B. Madore, K. S. Lee, T. A. Altes, D. A. Lynch, J. R. Mayo, J. B. Seo, *et al.*, “Expanding applications of pulmonary mri in the clinical evaluation of lung disorders: Fleischner society position paper,” *Radiology*, vol. 297, no. 2, pp. 286–301, 2020.
- [2] Y. Ohno, S. Hanamatsu, Y. Obama, T. Ueda, H. Ikeda, H. Hattori, K. Murayama, and H. Toyama, “Overview of mri for pulmonary functional imaging,” *The British Journal of Radiology*, vol. 95, no. 1132, p. 20201053, 2022.
- [3] M. Sharma, P. V. Wyszkievicz, V. Desai, Goudar, F. Guo, D. P. Capaldi, and G. Parraga, “Quantification of pulmonary functional mri: state-of-the-art and emerging image processing methods and measurements,” *Physics in Medicine & Biology*, vol. 67, no. 22, p. 22TR01, 2022.
- [4] F. Sanchez, P. N. Tyrrell, P. Cheung, C. Heyn, S. Graham, I. Poon, Y. Ung, A. Louie, M. Tsao, and A. Oikonomou, “Detection of solid and subsolid pulmonary nodules with lung mri: performance of ute, t1 gradient-echo, and single-shot t2 fast spin echo,” *Cancer Imaging*, vol. 23, no. 1, p. 17, 2023.
- [5] P. Larson, “Lung imaging with ute-mri,” in *MRI of Short-and Ultrashort-T2 Tissues: Making the Invisible Visible*, pp. 527–534, Springer, 2024.
- [6] X. Wang, Y. Cui, Y. Wang, S. Liu, N. Meng, W. Wei, Y. Bai, Y. Shen, J. Guo, Z. Guo, *et al.*, “Assessment of lung nodule detection and lung ct screening reporting and data system

- classification using zero echo time pulmonary mri,” *Journal of Magnetic Resonance Imaging*, vol. 61, no. 2, pp. 822–829, 2025.
- [7] F. Ufuk, B. Kurnaz, H. Peker, E. Sagtas, Z. D. Ok, and V. Cobankara, “Comparing three-dimensional zero echo time (3d-zte) lung mri and chest ct in the evaluation of systemic sclerosis-related interstitial lung disease,” *European Radiology*, pp. 1–10, 2024.
- [8] D. B. Gandhi, N. S. Higano, A. D. Hahn, C. C. Gunatilaka, L. A. Torres, S. B. Fain, J. C. Woods, and A. J. Bates, “Comparison of weighting algorithms to mitigate respiratory motion in free-breathing neonatal pulmonary radial ute-mri,” *Biomedical physics & engineering express*, vol. 10, no. 3, p. 035030, 2024.
- [9] N. Yu, H. Duan, C. Yang, Y. Yu, and S. Dang, “Free-breathing radial 3d fat-suppressed t1-weighted gradient echo (r-vibe) sequence for assessment of pulmonary lesions: a prospective comparison of ct and mri,” *Cancer Imaging*, vol. 21, pp. 1–9, 2021.
- [10] C. Wu, G. Krishnamoorthy, V. Yu, E. Subashi, A. Rimner, and R. Otazo, “4d lung mri with high-isotropic-resolution using half-spoke (ute) and full-spoke 3d radial acquisition and temporal compressed sensing reconstruction,” *Physics in Medicine & Biology*, vol. 68, no. 3, p. 035017, 2023.
- [11] K. M. Johnson, S. B. Fain, M. L. Schiebler, and S. Nagle, “Optimized 3d ultrashort echo time pulmonary mri,” *Magnetic resonance in medicine*, vol. 70, no. 5, pp. 1241–1250, 2013.
- [12] X. Zhu, F. Tan, K. Johnson, and P. Larson, “Optimizing trajectory ordering for fast radial ultrashort te (ute) acquisitions,” *Journal of Magnetic Resonance*, vol. 327, p. 106977, 2021.
- [13] Q. Zou, Z. Miller, S. Dzelebdzic, M. Abadeer, K. M. Johnson, and T. Hussain, “Time-resolved 3d cardiopulmonary mri reconstruction using spatial transformer network,” *Mathematical Biosciences and Engineering*, vol. 20, no. 9, pp. 15982–15998, 2023.
- [14] Q. Zou, “Motion-resolved 3d pulmonary mri reconstruction using sinusoidal representation networks,” *Current Medical Imaging*, vol. 20, no. 1, p. e15734056270732, 2024.
- [15] K. Montazeri, S. A. Jonsson, J. S. Agustsson, M. Serwatko, T. Gislason, and E. S. Arnardottir, “The design of rip belts impacts the reliability and quality of the measured respiratory signals,” *Sleep and Breathing*, pp. 1–7, 2021.
- [16] L. Feng, R. Grimm, K. T. Block, H. Chandarana, S. Kim, J. Xu, L. Axel, D. K. Sodickson, and R. Otazo, “Golden-angle radial sparse parallel mri: combination of compressed sensing, parallel imaging, and golden-angle radial sampling for fast and flexible dynamic volumetric mri,” *Magnetic resonance in medicine*, vol. 72, no. 3, pp. 707–717, 2014.
- [17] L. Feng, L. Axel, H. Chandarana, K. T. Block, D. K. Sodickson, and R. Otazo, “Xd-grasp: golden-angle radial mri with reconstruction of extra motion-state dimensions using compressed sensing,” *Magnetic resonance in medicine*, vol. 75, no. 2, pp. 775–788, 2016.
- [18] F. Ong, X. Zhu, J. Y. Cheng, K. M. Johnson, P. E. Larson, S. S. Vasanaawala, and M. Lustig, “Extreme mri: Large-scale volumetric dynamic imaging from continuous non-gated acquisitions,” *Magnetic resonance in medicine*, vol. 84, no. 4, pp. 1763–1780, 2020.
- [19] V. Murray, S. Siddiq, C. Crane, M. El Homsy, T.-H. Kim, C. Wu, and R. Otazo, “Movienet: deep space–time–coil reconstruction network without k-space data consistency for fast motion-resolved 4d mri,” *Magnetic resonance in medicine*, vol. 91, no. 2, pp. 600–614, 2024.
- [20] R. Jafari, R. K. G. Do, M. D. LaGratta, M. Fung, E. Bayram, T. Cashen, and R. Otazo, “Graspnet: fast spatiotemporal deep learning reconstruction of golden-angle radial data for free-breathing dynamic contrast-enhanced magnetic resonance imaging,” *NMR in Biomedicine*, vol. 36, no. 3, p. e4861, 2023.
- [21] Q. Zou, L. A. Torres, S. B. Fain, N. S. Higano, A. J. Bates, and M. Jacob, “Dynamic imaging using motion-compensated smoothness regularization on manifolds (moco-storm),” *Physics in medicine & biology*, vol. 67, no. 14, p. 144001, 2022.
- [22] K. Li, T. Pham, H. Zhan, and I. Reid, “Efficient dense point cloud object reconstruction using deformation vector fields,” in *Proceedings of the European Conference on Computer Vision (ECCV)*, pp. 497–513, 2018.

- [23] B. Kerbl, G. Kopanas, T. Leimkühler, and G. Drettakis, “3d gaussian splatting for real-time radiance field rendering,” *ACM Trans. Graph.*, vol. 42, no. 4, pp. 139–1, 2023.
- [24] J.-L. Bersillon, F. Villieras, F. Bardot, T. Gorner, and J.-M. Cases, “Use of the gaussian distribution function as a tool to estimate continuous heterogeneity in adsorbing systems,” *Journal of colloid and interface science*, vol. 240, no. 2, pp. 400–411, 2001.
- [25] R. Zha, T. J. Lin, Y. Cai, J. Cao, Y. Zhang, and H. Li, “R²-gaussian: Rectifying radiative gaussian splatting for tomographic reconstruction,” *arXiv preprint arXiv:2405.20693*, 2024.
- [26] X. Zhu, M. Chan, M. Lustig, K. M. Johnson, and P. E. Larson, “Iterative motion-compensation reconstruction ultra-short te (imoco ute) for high-resolution free-breathing pulmonary mri,” *Magnetic resonance in medicine*, vol. 83, no. 4, pp. 1208–1221, 2020.
- [27] T. Zhang, J. Y. Cheng, Y. Chen, D. G. Nishimura, J. M. Pauly, and S. S. Vasanawala, “Robust self-navigated body mri using dense coil arrays,” *Magnetic resonance in medicine*, vol. 76, no. 1, pp. 197–205, 2016.
- [28] M. Jaderberg, K. Simonyan, A. Zisserman, *et al.*, “Spatial transformer networks,” *Advances in neural information processing systems*, vol. 28, 2015.
- [29] P. Rodríguez, “Total variation regularization algorithms for images corrupted with different noise models: a review,” *Journal of Electrical and Computer Engineering*, vol. 2013, no. 1, p. 217021, 2013.
- [30] D. Charatan, S. L. Li, A. Tagliasacchi, and V. Sitzmann, “pixelsplat: 3d gaussian splats from image pairs for scalable generalizable 3d reconstruction,” in *Proceedings of the IEEE/CVF conference on computer vision and pattern recognition*, pp. 19457–19467, 2024.
- [31] J. Jung, J. Han, H. An, J. Kang, S. Park, and S. Kim, “Relaxing accurate initialization constraint for 3d gaussian splatting,” *arXiv preprint arXiv:2403.09413*, 2024.
- [32] T. Peng, R. Zha, Z. Li, X. Liu, and Q. Zou, “Three-dimensional mri reconstruction with gaussian representations: Tackling the undersampling problem,” *arXiv preprint arXiv:2502.06510*, 2025.
- [33] H. Pedersen, S. Kozerke, S. Ringgaard, K. Nehrke, and W. Y. Kim, “k-t pca: temporally constrained k-t blast reconstruction using principal component analysis,” *Magnetic Resonance in Medicine: An Official Journal of the International Society for Magnetic Resonance in Medicine*, vol. 62, no. 3, pp. 706–716, 2009.
- [34] M. K. Vairalkar and S. Nimbhorkar, “Edge detection of images using sobel operator,” *Int. J. Emerg. Technol. Adv. Eng*, vol. 2, no. 1, pp. 291–293, 2012.
- [35] X. Wang, “Laplacian operator-based edge detectors,” *IEEE transactions on pattern analysis and machine intelligence*, vol. 29, no. 5, pp. 886–890, 2007.
- [36] T.-Y. Lin, P. Dollár, R. Girshick, K. He, B. Hariharan, and S. Belongie, “Feature pyramid networks for object detection,” in *Proceedings of the IEEE conference on computer vision and pattern recognition*, pp. 2117–2125, 2017.
- [37] W.-S. Lai, J.-B. Huang, N. Ahuja, and M.-H. Yang, “Fast and accurate image super-resolution with deep laplacian pyramid networks,” *IEEE transactions on pattern analysis and machine intelligence*, vol. 41, no. 11, pp. 2599–2613, 2018.
- [38] Z. Yan, W. F. Low, Y. Chen, and G. H. Lee, “Multi-scale 3d gaussian splatting for anti-aliased rendering,” in *Proceedings of the IEEE/CVF Conference on Computer Vision and Pattern Recognition*, pp. 20923–20931, 2024.
- [39] R. Li and Y.-m. Cheung, “Variational multi-scale representation for estimating uncertainty in 3d gaussian splatting,” *Advances in Neural Information Processing Systems*, vol. 37, pp. 87934–87958, 2024.
- [40] Z. Yu, A. Chen, B. Huang, T. Sattler, and A. Geiger, “Mip-splatting: Alias-free 3d gaussian splatting,” in *Proceedings of the IEEE/CVF Conference on Computer Vision and Pattern Recognition*, pp. 19447–19456, 2024.
- [41] J. Zhang, F. Zhan, M. Xu, S. Lu, and E. Xing, “Fregs: 3d gaussian splatting with progressive frequency regularization,” in *Proceedings of the IEEE/CVF Conference on Computer Vision and Pattern Recognition*, pp. 21424–21433, 2024.

- [42] R. C. Gonzalez, *Digital image processing*. Pearson education india, 2009.